

# A Family of Multi-Dimensional Thermal Radiative Transfer Test Problems

Thomas A. Brunner  
Lawrence Livermore National Laboratory  
LLNL-TR-858450

December 2023

## 1 Introduction

Many thermal radiative transfer (TRT) test problems have been introduced over the years. Here, we will combine the good features of several tests into one new problem. Our goals are to have a multi-dimensional, multi-group TRT problem that stresses the physics and numerics of codes in a realistic way, but the geometry and materials are idealized just enough to be simple to set up in any code. The proposed problem has no connection to any physical experiment; it is simply meant to have a combination of properties that stress the solvers with both the optically thick and thin limits. To achieve this, we are willing to give up any form of analytic solution.

We will also define a family of problems that capture the essence of the full physics, but simplify the problem to neutral-particle transport only without material coupling, a steady state variant, and more. We will define a two-dimensional Cartesian, a two dimensional cylindrical, and a three-dimensional Cartesian variant. We also provide reference solutions to this problem with some quantities of interest for comparison.

## 2 Thermal Radiative Transport

We wish to define our test problem for a simplified thermal radiative transfer system, where a multi-frequency photon transport is coupled to a material energy equation. The simplified frequency-dependent equations[5] without physical scattering are given by

$$\frac{1}{c} \frac{\partial \psi}{\partial t} = -\mathbf{\Omega} \cdot \nabla \psi - \sigma \psi + \sigma B, \quad (1)$$

$$\rho c_v \frac{\partial T}{\partial t} = \int \sigma [\phi - 4\pi B] d\epsilon, \text{ and} \quad (2)$$

$$B(\epsilon, T) = \frac{2k^4}{c^2 h^3} \frac{\epsilon^3}{e^{\epsilon/T} - 1}, \quad (3)$$

where  $B$  is the Planck function. See Appendix B for deriving this form from the more common frequency dependent version. We can discretize in photon energy to get the multigroup equation, namely

$$\frac{1}{c} \frac{\partial \psi_g}{\partial t} = -\mathbf{\Omega} \cdot \nabla \psi_g - \sigma_{P,g} \psi_g + \sigma_{P,g} B_g, \quad (4)$$

$$\rho c_v \frac{\partial T}{\partial t} = \sum_g \sigma_{P,g} \phi_g - \sum_g \sigma_{P,g} 4\pi B_g, \quad (5)$$

$$\psi_g(\mathbf{x}, \mathbf{\Omega}) = \int_{\epsilon_{g-1/2}}^{\epsilon_{g+1/2}} \psi(\mathbf{x}, \mathbf{\Omega}, \epsilon) d\epsilon, \quad (6)$$

$$\phi_g(\mathbf{x}) = \int_{4\pi} \psi_g(\mathbf{x}) d\mathbf{\Omega}, \quad (7)$$

$$B_g(T) = \int_{\epsilon_{g-1/2}}^{\epsilon_{g+1/2}} B(\epsilon, T) d\epsilon = \int_{\epsilon_{g-1/2}}^{\epsilon_{g+1/2}} \frac{2k^4}{c^2 h^3} \frac{\epsilon^3}{e^{\epsilon/T} - 1} d\epsilon, \text{ and} \quad (8)$$

$$\sigma_{P,g}(T, \rho) = \frac{1}{B_g(T)} \int_{\epsilon_{g-1/2}}^{\epsilon_{g+1/2}} \sigma(T, \rho, \epsilon) B(T, \epsilon) d\epsilon. \quad (9)$$

All variables and physical constants, along with their units can be found in Tab. 1. We call  $\sigma_{P,g}$  the Planck-weighted group averaged opacity. Note that sometimes the specific opacity is used and has units of  $\text{cm}^2 \text{g}^{-1}$ . Often it is also represented by the symbol  $\sigma$ . Here we distinguish these by using  $\kappa$  to designate the specific opacity, and  $\sigma = \rho \kappa$  to be the inverse mean free path of the photon.

Near equilibrium when the radiation field is mostly isotropic, Eq. 1 and Eq. 4 can be approximated using a diffusion approximation[5, 3]. With this we get

$$\frac{1}{c} \frac{\partial \phi}{\partial t} - \nabla \cdot \frac{1}{3\sigma} \nabla \phi = -\sigma \phi + 4\pi \sigma B, \quad (10)$$

To average the diffusion term accurately in the thick limit, we can assume the radiation is nearly in equilibrium with the material,

$$\int_{\epsilon_{g-1/2}}^{\epsilon_{g+1/2}} \nabla \cdot \frac{1}{3\sigma} \nabla 4\pi B(T) d\epsilon \approx \int_{\epsilon_{g-1/2}}^{\epsilon_{g+1/2}} \nabla \cdot \frac{1}{3\sigma} 4\pi \frac{\partial B(T)}{\partial T} \nabla T d\epsilon = \nabla \cdot 4\pi \left[ \int_{\epsilon_{g-1/2}}^{\epsilon_{g+1/2}} \frac{1}{3\sigma} \frac{\partial B(T)}{\partial T} d\epsilon \right] \nabla T \quad (11)$$

We can define the Rosseland average from this as

$$\sigma_{R,g} = \int_{\epsilon_{g-1/2}}^{\epsilon_{g+1/2}} \frac{\partial B(T)}{\partial T} d\epsilon \bigg/ \int_{\epsilon_{g-1/2}}^{\epsilon_{g+1/2}} \frac{1}{\sigma} \frac{\partial B(T)}{\partial T} d\epsilon. \quad (12)$$

With this, we get

$$\frac{1}{c} \frac{\partial \phi_g}{\partial t} - \nabla \cdot \frac{1}{\sigma_{R,g}} \nabla \phi_g = -\sigma_{P,g} \phi_g + 4\pi \sigma_{P,g} B_g. \quad (13)$$

Eq. 13 implies that we want to use both the Rosseland and Planck averages while solving the diffusion equation. But in Eq. 4, there is only one opacity present. While it would seem the Planck average is appropriate, we often use the Rosseland mean free path for all group-averaged opacities in both the diffusion and transport equations.

Other useful quantities are the total radiation energy density, which is defined by integrating over all photon energies and angles to get

$$u_r = \frac{1}{c} \int_{4\pi} \int_0^\infty \psi d\epsilon d\mathbf{\Omega}. \quad (14)$$

Table 1: Nomenclature and Units

Symbol	Name	units
$\mathbf{x}$	position	cm
$t$	time	s
$\epsilon$	photon energy	keV
$\Omega$	direction of photon travel	unitless
$\psi(\mathbf{x}, \Omega, \epsilon, t)$	radiation intensity	erg/cm <sup>2</sup> s sr keV
$\phi(\mathbf{x}, \epsilon, t)$	angle integrated intensity	erg/cm <sup>2</sup> s keV
$T(\mathbf{x}, t)$	material temperature	keV
$\rho(\mathbf{x})$	density	g/cm <sup>3</sup>
$c_v(\mathbf{x}, T, \rho)$	specific heat	erg/g keV
$\sigma(\mathbf{x}, T, \rho, \epsilon)$	absorption opacity	cm <sup>-1</sup>
$u$	energy density	erg/cm <sup>3</sup>
$p$	pressure	erg/cm <sup>3</sup>
$g$	group index	unitless
$\psi_g(\mathbf{x}, \Omega, t)$	group-integrated radiation intensity	erg/cm <sup>2</sup> s sr
$\phi_g(\mathbf{x}, t)$	group-integrated radiation intensity	erg/cm <sup>2</sup> s
$\sigma_{P,g}(\mathbf{x}, T, \rho)$	Planck-weighted group average absorption opacity	cm <sup>-1</sup>
$\sigma_{R,g}(\mathbf{x}, T, \rho)$	Rosseland-weighted group average absorption opacity	cm <sup>-1</sup>
$\kappa_x = \sigma_x / \rho$	Specific opacity of any flavor	cm <sup>2</sup> g <sup>-1</sup>
$c$	speed of light	$2.99792458 \cdot 10^{10}$ cm/s
$h$	Planck constant	$6.62607015 \cdot 10^{-27}$ erg s
$k$	Boltzmann constant	$1.602176634 \cdot 10^{-9}$ erg/keV
$a$	radiation constant	$1.3720169264801069 \cdot 10^{14}$ erg/cm <sup>3</sup> keV <sup>4</sup>
$N_A$	Avogadro constant	$6.02214076 \cdot 10^{23}$ mol <sup>-1</sup>
$A$	atomic mass	g/mol
$Z_{\text{eff}}$	effective ionization state	unitless

In equilibrium when  $\psi = B$ , we have

$$\hat{u}_r = \frac{1}{c} \int_{4\pi} \int_0^\infty B(\epsilon, t) d\epsilon d\Omega = aT^4 \quad (15)$$

$$a = \frac{8\pi^5 k^4}{15c^3 h^3} = \frac{4\sigma_{\text{SB}}}{c}, \quad (16)$$

where  $a$  is the radiation constant and  $\sigma_{\text{SB}}$  is the Stefan-Boltzmann constant. In non-equilibrium cases, it is often convenient to compare the material temperature to a radiation temperature defined by

$$T_r = \left( \frac{u_r}{a} \right)^{1/4}. \quad (17)$$

It will also be useful to factor the frequency integrated Planck function as

$$B_g(T) = \int_{\epsilon_{g-1/2}}^{\epsilon_{g+1/2}} \frac{2k^4}{c^2 h^3} \frac{\epsilon^3}{e^{\epsilon/T} - 1} d\epsilon = \frac{2\pi^4 k^4 T^4}{15c^2 h^3} \int_{\epsilon_{g-1/2}}^{\epsilon_{g+1/2}} \frac{15}{\pi^4} \frac{\epsilon^3}{T^3} \frac{1}{e^{\epsilon/T} - 1} \frac{d\epsilon}{T} = \frac{2\pi^4 k^4 T^4}{15c^2 h^3} b_g(T) = \frac{ca}{4\pi} b_g(T) \quad (18)$$

where

$$b_g(T) = \int_{\epsilon_{g-1/2}}^{\epsilon_{g+1/2}} \frac{15}{\pi^4} \frac{\epsilon^3}{T^3} \frac{1}{e^{\epsilon/T} - 1} \frac{d\epsilon}{T}. \quad (19)$$

This new function,  $b_g$  represents the fraction of energy of the total Planck function in a given group. If we integrate from zero to infinity,  $b_g$  is one. We will also want the normalized derivative of  $b_g$  later. This can be written as

$$\frac{\partial b_g(T)}{\partial T} = \int_{\epsilon_{g-1/2}}^{\epsilon_{g+1/2}} \frac{15}{\pi^4} \frac{\epsilon^4}{T^4} \frac{e^{\epsilon/T}}{(e^{\epsilon/T} - 1)^2} \frac{d\epsilon}{T}. \quad (20)$$

### 3 Currently defined problems

One common multi-dimensional problem is the Crooked Pipe problem [12, 10]. This problem has many of the challenging geometric features, but has several critical drawbacks. The first is that the official definition is only for grey transport, with constant opacities material properties. It is also driven by a boundary condition. This tends to cause one small part of the spatial domain to control the problem, and does not stress the full solver until much later into the run.

The Straight Pipe problem [15] has a slightly simplified geometry and did extend the materials to have frequency dependent opacities. However, these opacities and the emission within a group tend to go to infinity as you get closer to zero frequency, which makes the problem very sensitive to the lower group bound.

The Prompt Radiating Sphere problem [11] problem has an analytic solution for any opacity. This is very useful for code verification. However, the material is not allowed to heat up, and it does not stress the nonlinear solvers at all.

Su and Olson [16] developed also multigroup test problem with an analytic solution. In this problem, the material can heat, but the opacities and specific heat of the material are defined in such a way that convert the problem into a linear one that allows the analytic solution, which makes testing nonlinear solvers difficult.

In [13, 6, 7], Larsen defined a one-dimensional frequency problem with realistic opacities. This problem was designed to stress the linear and nonlinear solvers in realistic ways. The group averaged opacities stay finite for any set of group bounds and have a form that can be integrated analytically.

In [17], Till proposed a problem based on an experiment at the Omega facility. This problem is very close to what we'd like, but it is only specified using real materials. It also is purely boundary driven, much like the pipe problems, which means it takes a while for the problem to reach what we'll call an algorithmic steady-state.

In [3], the author used a simple lattice-like geometry that has been extended to grey radiative transfer in [14]. We propose extending this problem further to use analytic opacities similar to the ones of Larsen [13].

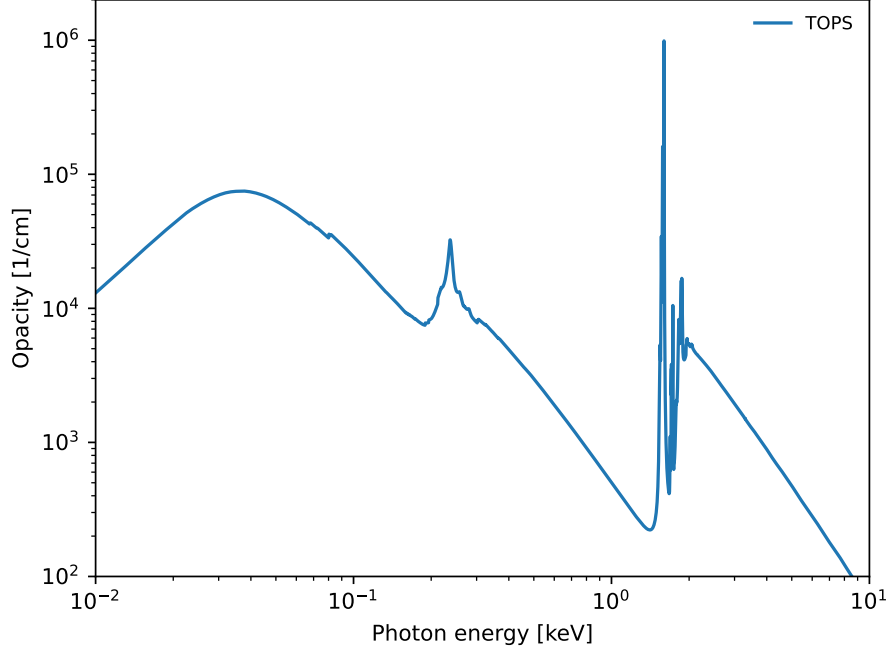


Figure 1: Frequency dependent opacity for aluminum at  $T = 0.25$  keV and  $\rho = 2.7$  g/cm<sup>3</sup>

## 4 Analytic Material Properties

We will first describe the general form of our material properties before describing specific parameters to use in our test problem.

### 4.1 Opacities

Fig. 1 shows a typical frequency dependent absorption opacity from [1]. Our goal is to create approximate opacities that have the realistic scaling behavior with density, temperature, and frequency, and also include some of the features that make computing a group-converged answer difficult. A non-goal is to perfectly match any real opacity; we want to stress the numerical methods in similar ways to real opacities while being easy to describe and set up in any code.

We start with Eq. 2.7 in [13], where Larsen proposed the analytic frequency dependent opacity

$$\sigma_L = C_0 \frac{\rho^2}{\sqrt{T} \epsilon^3} \left(1 - e^{-\epsilon/T}\right). \quad (21)$$

This is based on Eq. 5.21 in [20], but includes corrections for simulated emission[6]. We will extend this with three more features that can be seen in Fig. 1.

The first is the ability to have shell edges. An example of this can be seen at  $\epsilon \approx 2$  keV in Fig. 1. Often, there is a large jump in opacity for photons that have enough energy to excite a new ionization state of the material. We will approximate this feature by an extra multiplicative factor that includes a Heaviside step function, denoted by

$$H(x) = \begin{cases} 1 & x \geq 0 \\ 0 & x < 0 \end{cases}. \quad (22)$$

The second modification will be to further limit the opacity at low photon energy. In real materials, there are often collective effects that change the form of the opacity in such a way that is not captured by Eq. 21. This can be seen in Fig. 1 at  $\epsilon \approx 0.04$  keV where the opacity starts to decline as the photon energy falls off. We will accomplish this by simply putting a lower bound on the value of  $\epsilon$  in the evaluation of the formula.

The third and final modification we will make is to add narrow line-like features, seen in Fig. 1 just below the shell edge and also near  $\epsilon \approx 0.27$  keV. We are going to approximate these by adding a series of Gauss functions[18] near the shell edge.

This makes the final parameterized form of our opacity to be

$$\hat{\epsilon} = \max(\epsilon_{\min}, \epsilon) \quad (23)$$

$$\sigma(\epsilon, T, \rho) = C_0 \frac{\rho^2}{\sqrt{T} \hat{\epsilon}^3} \left[ 1 - e^{-\hat{\epsilon}/T} \right] \left[ 1 + C_1 H(\hat{\epsilon} - \epsilon_{\text{edge}}) + \sum_{l=0}^{N_l-1} \frac{C_2}{N_l - l} \exp \left( -\frac{1}{2} \left[ \frac{\hat{\epsilon} - (\epsilon_{\text{edge}} - (l+1)\delta_s)}{\delta_w} \right]^2 \right) \right], \quad (24)$$

where  $C_0$ ,  $C_1$ , and  $C_2$  are values that scale the overall opacity, the edge feature, and the line features respectively,  $\epsilon_{\min}$  defines the low frequency cutoff,  $\epsilon_{\text{edge}}$  defines the location of the shell edge,  $N_l$  is the number of line features,  $\delta_w$  is the width of each line,  $\delta_s$  is the separation of each of the lines starting from the edge and moving downward.

While it is possible, without the line features, to analytically integrate the Planck-weighted group averaged opacities, assuming you can calculate  $b_g$  in some other way, we have opted to numerically integrate the opacities. This allows us to compute both Rosseland- and Planck-weighted averages as well as normalized Planck  $b_g$  and Rosseland  $\partial b / \partial T$  functions for each group. Relatively simple Gaussian integration is performed over subregions of the opacity that matches the features in Eq. 24. While we will not discuss the details of this integration, there is a companion release[2] of C++ code to evaluate the frequency dependent opacity and a numeric integrator to compute the Rosseland and Planck multigroup (and grey) opacities. The details of the algorithm are contained in the source code itself.

## 4.2 Equation of State

We will use the ideal gas law to define the equation of state for the materials. In this model, we have

$$p = \frac{N_A(Z_{\text{eff}} + 1)}{A} \rho k T, \quad (25)$$

where the factor of  $(Z_{\text{eff}} + 1)$  accounts for the number of free electrons plus the ion in the gas. We will treat the ionization state as a constant in this work, but this is one of the most important reasons that the specific heat of real materials is not constant. The internal energy density of an ideal gas, assuming three degrees of freedom, is given by

$$u = \frac{3}{2} \frac{N_A(Z_{\text{eff}} + 1)}{A} \rho k T = \rho c_v T, \quad (26)$$

$$c_v = \frac{3}{2} \frac{k N_A(Z_{\text{eff}} + 1)}{A} \quad (27)$$

## 5 The Lattice Problem

We now turn to the specific test problem definition. The main idea is to have a simple lattice of hot and cold materials on the mesh, spanning the optically thin to optically thick range. The geometry is loosely based on the lattice problems either [3] or [14].

Table 2: Material locations, densities, and initial temperatures

Material Name	Initial Temperature	Density	Left Boundary	Right Boundary	Bottom Boundary	Top Boundary
foam	0.001 keV	0.2 g/cm <sup>3</sup>	entire box, replaced by other materials			
carbon	0.001 keV	2.0 g/cm <sup>3</sup>	2 cm	3 cm	2 cm	3 cm
carbon	0.001 keV	2.0 g/cm <sup>3</sup>	2 cm	3 cm	4 cm	5 cm
carbon	0.001 keV	2.0 g/cm <sup>3</sup>	3 cm	4 cm	1 cm	2 cm
carbon	0.001 keV	2.0 g/cm <sup>3</sup>	3 cm	4 cm	5 cm	6 cm
carbon	0.001 keV	2.0 g/cm <sup>3</sup>	4 cm	5 cm	2 cm	3 cm
carbon	0.001 keV	2.0 g/cm <sup>3</sup>	4 cm	5 cm	4 cm	5 cm
cold iron	0.001 keV	6.0 g/cm <sup>3</sup>	1 cm	2 cm	1 cm	2 cm
cold iron	0.001 keV	6.0 g/cm <sup>3</sup>	1 cm	2 cm	5 cm	6 cm
cold iron	0.001 keV	6.0 g/cm <sup>3</sup>	5 cm	6 cm	1 cm	2 cm
cold iron	0.001 keV	6.0 g/cm <sup>3</sup>	5 cm	6 cm	5 cm	6 cm
hot iron	0.5 keV	8.0 g/cm <sup>3</sup>	3 cm	4 cm	3 cm	4 cm

## 5.1 Geometry

We intend this to be a family of test problems. We will define a material layout in a plane. This can be run in two-dimensional Cartesian geometry (XY), or revolved around the axis to form rings in a two-dimensional cylindrical geometry (RZ). It can be rotated around an axis or extruded out of the plane to make a three-dimensional Cartesian problem. The rotated 3D geometry should match the RZ version. The extruded geometry, if reflecting boundary conditions are employed on the faces perpendicular to the Z-axis, should match the XY geometry solutions.

The geometry is defined on a seven by seven centimeter box. Most of the problem starts at an initial temperature of  $T_{\text{cold}} = 0.001$  keV. The top and right boundaries have an incoming, isotropic Planck source at  $T_{\text{cold}}$ . The bottom boundary is reflecting in cylindrical geometry. The left boundary is an isotropic incoming source of  $T_{\text{hot}} = 1.0$  keV. These boundary conditions should ensure that the material or radiation temperature never falls below  $T_{\text{cold}}$ , unlike problems with vacuum boundaries. In fact, with this problem definition both the material and radiation temperatures should be bounded by  $T_{\text{cold}} \leq T_r, T \leq T_{\text{hot}}$  for all points in the domain for the entire simulation.

The materials are very loosely based on parameters for iron and carbon at different densities. While we will name each material a physical sounding name (like foam), there is at best a tenuous connection to reality. We are using the names only as easy to recognize monikers.

The background material is a low-density carbon foam. The radiation propagates through this material relatively easily with lots of streaming effects. There are eleven blocks (or rings) of material arranged in a lattice in the box. There are six high-density carbon blocks and four iron blocks that are initialized to  $T_{\text{cold}}$  at  $t = 0$ . One iron block in the middle is initialized at  $T_{\text{hot}}/2$ . This ensures that more of the mesh has radiation from time zero. With some of the material already hot within the volume of the problem, nonlinear solvers should be stressed consistently for the entire simulation without the usual “warm-up” period in problems driven purely by boundary conditions.

The exact locations, densities, and initial temperatures are shown in Tab. 2, while the problem is shown graphically in Fig. 2.

### 5.1.1 Meshing

The meshing is *not* part of the problem specification. Each code has unique capabilities. You should always perform your own mesh convergence study to assess if your solution is converged.

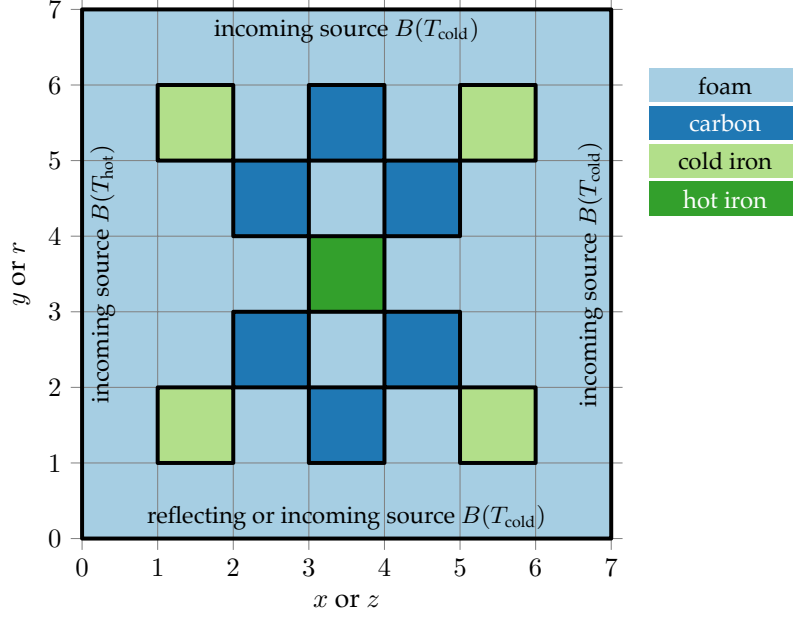


Figure 2: Lattice problem geometry

Table 3: Equation of state parameters for each material

material	density	$Z_{\text{eff}}$	atomic mass, $A$	specific heat, $c_v$
hot iron	8.0	20	56	5.4273e+14
cold iron	6.0	20	56	5.4273e+14
carbon	2.0	1	12	2.41213e+14
foam	0.2	1	12	2.41213e+14

## 5.2 Material Properties

Table 3 shows the parameters for the ideal gas specific heat model in Eq. 27. Table 4 shows the parameters in Eq. 24 for each material. A minimal set of sixteen groups was chosen, shown in Tab. 5. The  $\epsilon_{\text{min}}$  and  $\epsilon_{\text{edge}}$  from each opacity model are included. Extra points were added between these to maintain roughly equal logarithmic spacing across the range. No attempt was made to resolve the line features. This means the difference between the Rosseland and Planck averaged opacities can be larger than an order of magnitude. How each opacity behaves can be seen in Figures 3-6. Also included on the figures is the Planck function and its temperature derivatives which are used in the weighting functions of computing the multigroup averages.

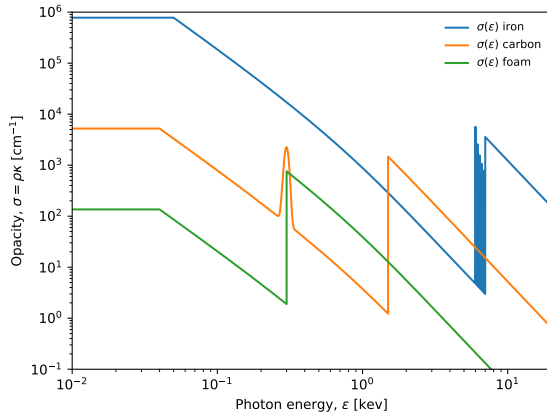
Table 4: Opacity parameters properties for each material

material	$\epsilon_{\text{min}}$ keV	$\epsilon_{\text{edge}}$ keV	$C_0$ $\text{cm}^5\text{keV}^{3.5}/\text{g}^2$	$C_1$ unitless	$C_2$ unitless	$N_l$ unitless	$\delta_w$ keV	$\delta_s$ keV
hot/cold iron	0.05	7.0	4.1	1.2e3	1.2e3	5	0.01	0.2
carbon	0.04	1.5	0.77.0	1.2e3	30	1	0.1	1.2
foam	0.04	0.3	8.0	4.0e2	0	0	0	0

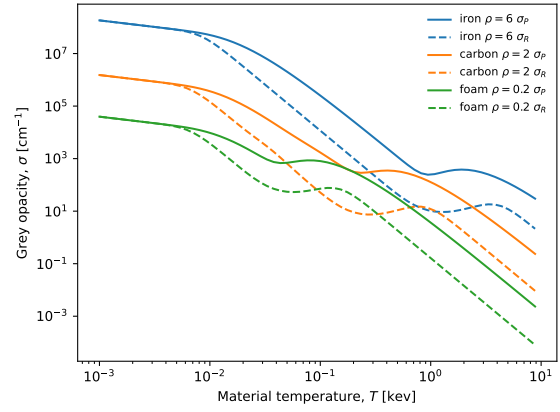


Table 5: Group Bounds

Edge Value (keV)
0.0001
3.0e-03
1.095445115010333e-02
4.0e-02
5.0e-02
7.825422900366437e-02
1.224744871391589e-01
1.916829312738817e-01
3.0e-01
6.708203932499368e-01
1.5e+00
3.240370349203930e+00
7.0e+00
1.114619555925213e+01
1.774823934929885e+01
2.826076380281411e+01
4.5e+01

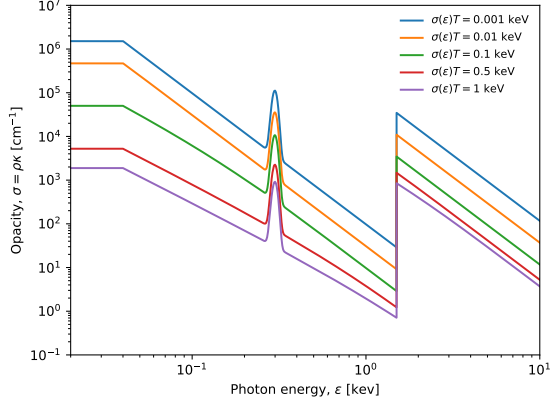


(a) Detailed opacities at  $T = 0.5$  keV

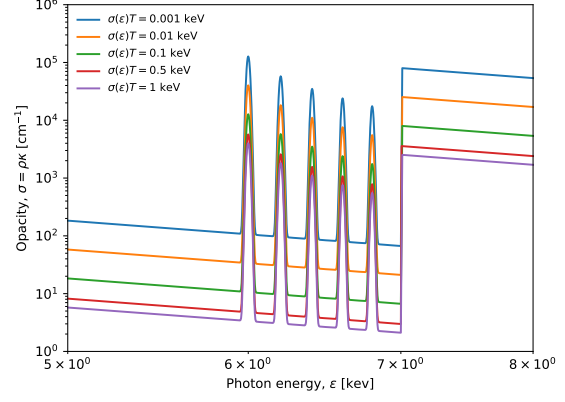


(b) Grey opacities

Figure 3: Opacity models for all three materials.

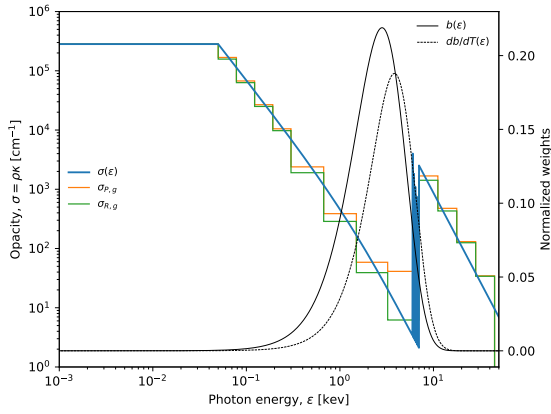


(a) Carbon detail

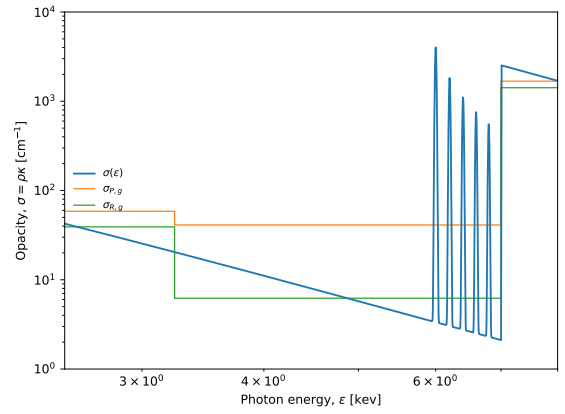


(b) Iron detail

Figure 4: Opacity features of carbon and iron at various temperatures



(a) Full range



(b) Detail range

Figure 5: Multigroup opacities for iron at  $T = 1.0$  keV

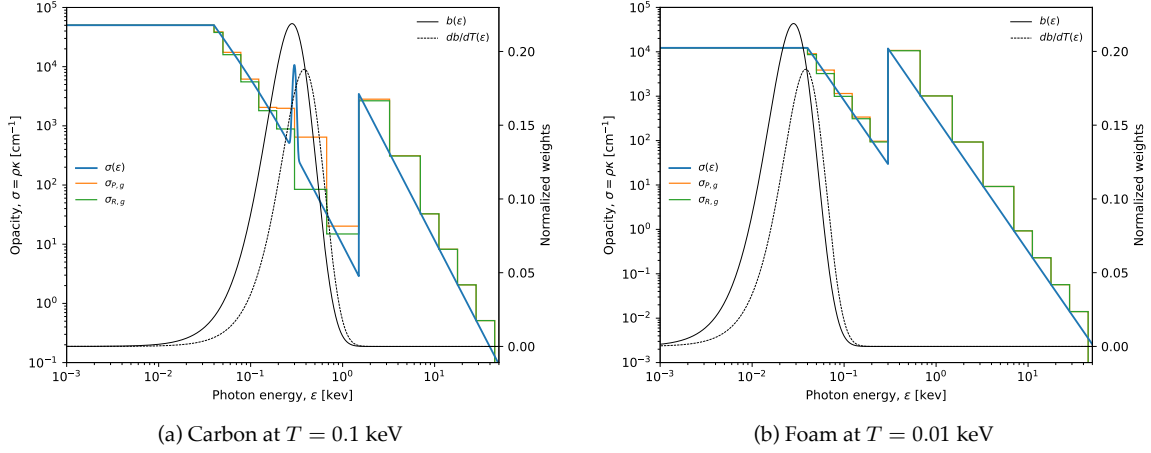


Figure 6: Multigroup opacities for carbon and foam

Table 6: Method details

Moniker	Details
IMC	A Fleck and Cummings based Implicit Monte Carlo[9, 19] with about 500 particles per zone per group per time step.
S8x8	A discrete ordinates[17] method using an 8 by 8 product quadrature for each quadrant in RZ for a total of $8 \cdot 8 \cdot 4 = 256$ angles per group.
S4x4	A discrete ordinates method using an 4 by 4 product quadrature for each quadrant in RZ for a total of $4 \cdot 4 \cdot 4 = 64$ angles per group.
MGFLD	A multigroup flux limited diffusion[15, 4] using the Max flux limiter.
FLD	A grey flux limited diffusion[15] using the Max flux limiter.

## 6 Results

The results shown here are to illustrate what to look for in the problem. No formal mesh or energy group resolution study was performed to check for convergence. While meshing is *not* part of the problem specification, the results here were run on a non-uniformly spaced Cartesian mesh with a total of 47089 zones in cylindrical geometry. Each centimeter square of material has a 31 by 31 grid of zones, distributed so they are closer to the edge of each square. This mesh is shown in Fig. 7. The odd number of zones allows us to put a tracer particle directly in the middle of each block that is only in one zone.

The simulation was run to 100 ns, which is almost long enough to reach steady state, but not quite. The problem undergoes some rapid transients in the first few nanoseconds and then slows as time progresses. The multiple time scales seen here are typical in many problems involving radiation transport.

Multiple methods were used to compute the solutions. This included grey diffusion, multigroup diffusion, discrete ordinates, and Implicit Monte Carlo (IMC)[3, 15, 17, 4, 9, 5]. We will not go into the details of the methods here. Some of the specifics for these runs are shown in Tab. 6. All of the well-known strengths and weaknesses of each method are highlighted in this problem.

Figs. 8-13 show the spatial evolution of the radiation temperature and material temperature from near the beginning of the problem through about 15 ns. In all of the figures, the difference between grey diffusion and multigroup diffusion is stark. High-energy photons see a lower opacity and stream ahead of the main

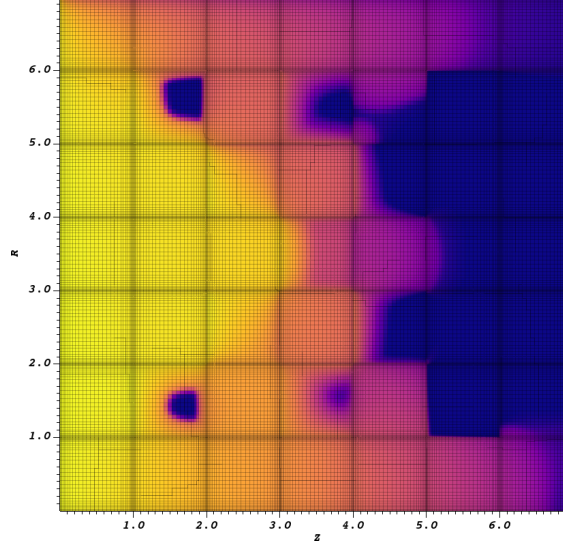


Figure 7: The material temperature at  $t = 2.0$  ns on a 47089 zone mesh with geometrically grid lines concentrated on the boundaries of each block

Marshak wave, pre-heating the material. This is one of the key differences typically seen between grey and multigroup calculations, and this new test problem illustrates that. Fig. 8 shows the radiation temperature at  $t = 0.1$  ns, and light has only had enough time to travel about 3 cm. We can see that IMC respects this with a sharp wave front of photons that have traveled from the left boundary without any collisions. But we can also see the usual noise that plagues IMC simulations. The discrete ordinate solution, however, is noise-free, but the classic ray-effects are visible. The discrete ordinates, along with the diffusion, also suffer from diffusion of the photon wave front because of the backward Euler time differencing method used. Both the discrete ordinates and the IMC methods keep sharp shadows when the radiation is blocked by a thicker material, with the diffusion method allows radiation to bleed around the corners much too quickly. In Fig. 10, the consequences of this can be seen. The diffusion method essentially heats the thick blocks of iron and carbon from all sides, so they heat much more rapidly than in the full transport method simulations.

Fig. 14 shows material properties typically seen in this problem. This first is the grey Rosseland opacity found by integrating Eq. 12 from zero to infinity. The opacity can span eight orders of magnitude across the problem, and must be handled dynamically by any multigroup method to remain robust. The photons can have a very short mean free path to essentially free streaming. Another way to look at this is through the Fleck factor, Eq. 31 in Appendix A, which is a term that appears in any linearization of Eqs. 4-5. The fraction of photons absorbed and remitted (or emitted and reabsorbed) during a step is given by  $1 - f$ . In this problem the thick regions that are heating rapidly can have a re-absorption fraction nearing 95%. This implicit or pseudo scattering can cause very slow convergence if not addressed[8, 13]. Fig. 15 shows the different nondimensional ratios that go into the Fleck factor, namely the ratio of the specific heats  $\beta$  (Eq. 32), and the ratio of path lengths  $\gamma$  (Eq. 33). For the pseudo scattering from linearization to be important, two things need to be true. The first is that the radiation field has to have enough energy in it to appreciably change the material energy. This is measured by  $\beta$ . The second is that the photon has to have a reasonable chance of being absorbed in this time step. This is measured by  $\gamma$ . Similarly, the re-emission source strength is proportional to  $\sigma_P T^3$ , so that is also plotted. These terms distill the complicated relationship between time step size, opacity values, and heat capacity that cause challenges for thermal radiation solvers, and care must be taken to choose representative values.

Fig. 16 shows the mesh-integrated internal (or thermal) and radiation energy in the problem. Because the boundaries are open, different amounts of energy enter the problem as we reach steady state. Another way to look at this same information is looking at the rate of energy exchange rather than the cumulative

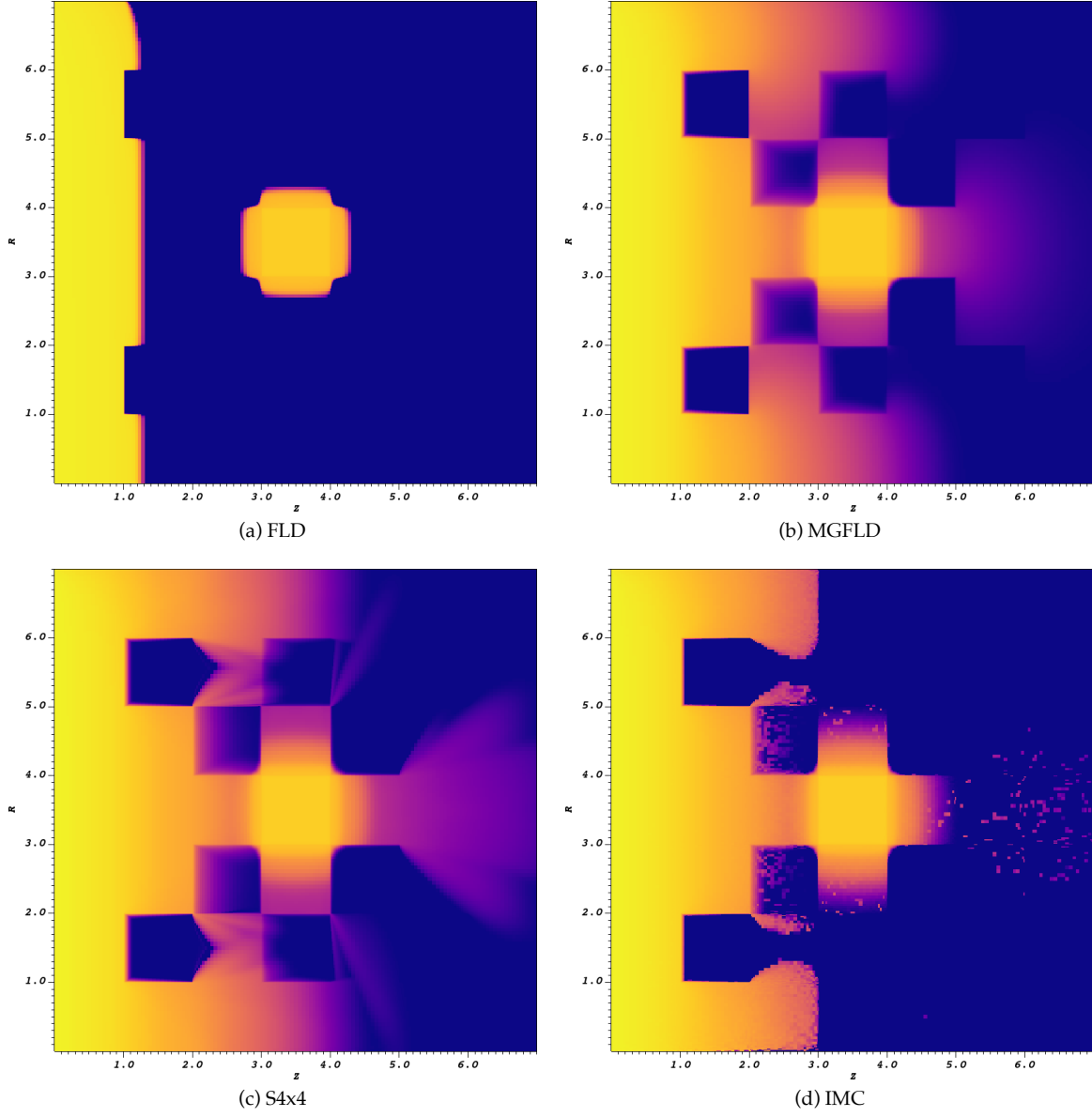
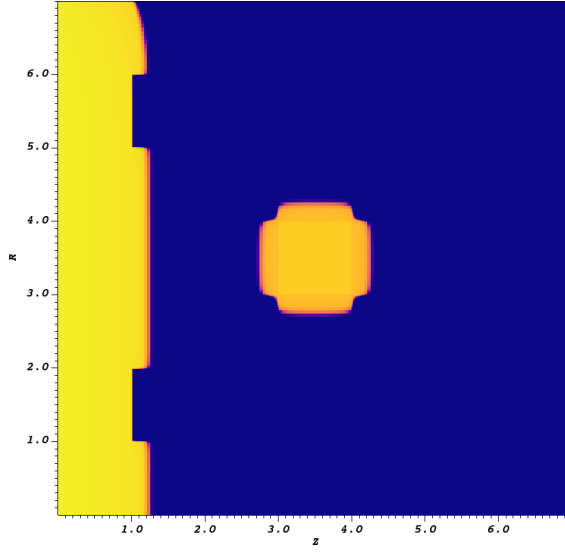
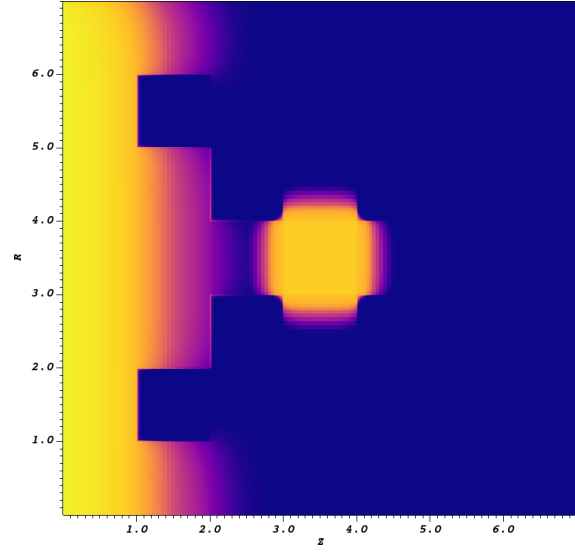


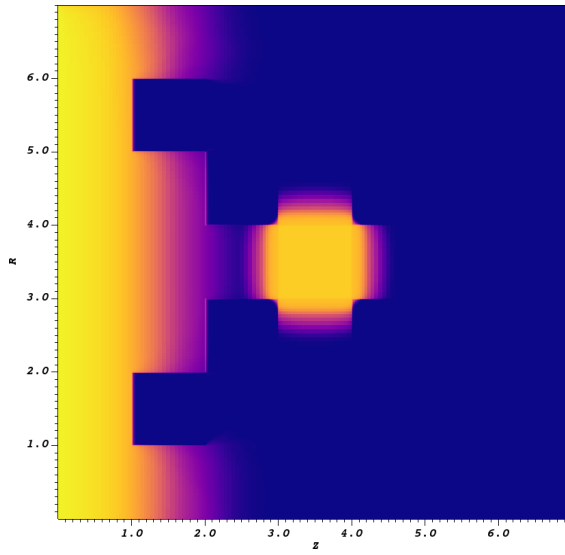
Figure 8: Log scale radiation temperature at  $t = 0.1$  ns for each method



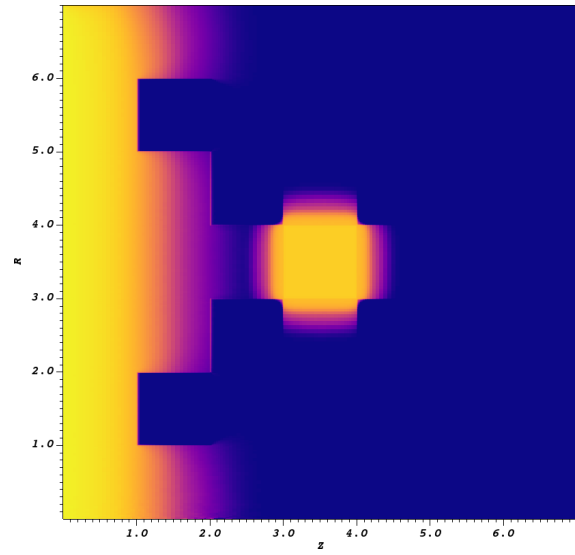
(a) FLD



(b) MGFLD



(c) S4x4



(d) IMC

Figure 9: Log scale material temperature at  $t = 0.1$  ns for each method

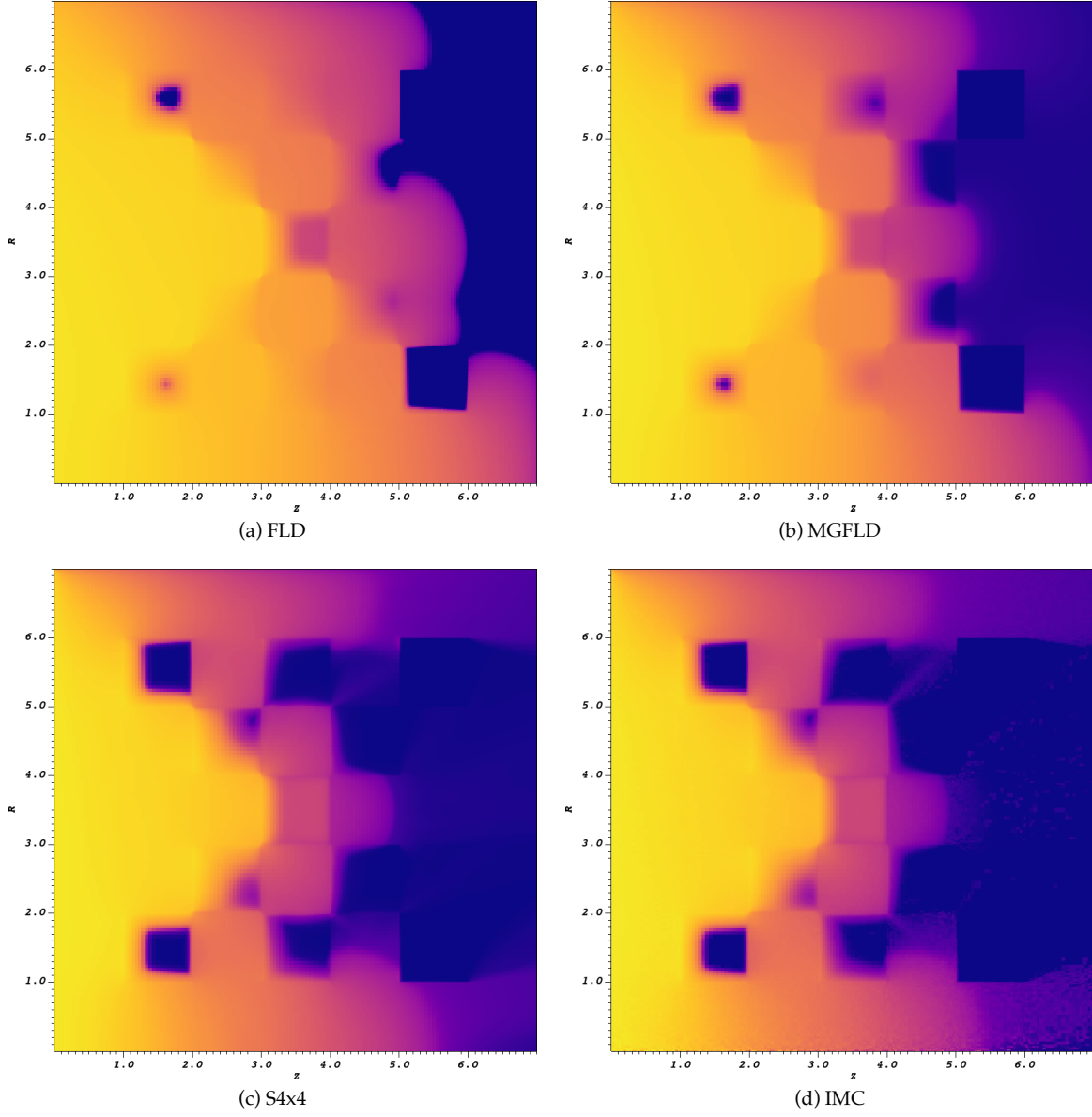
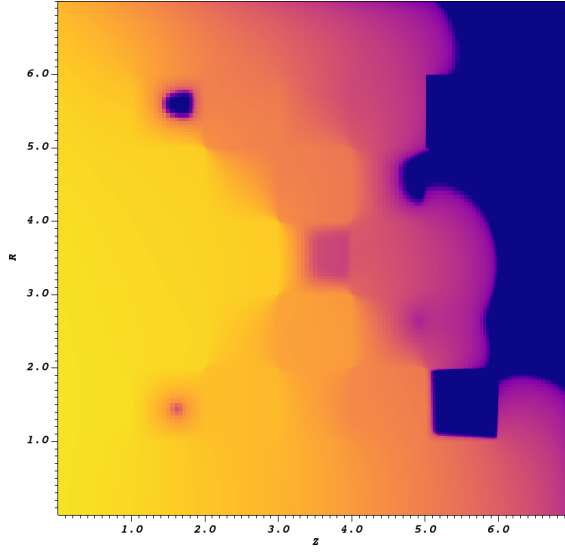
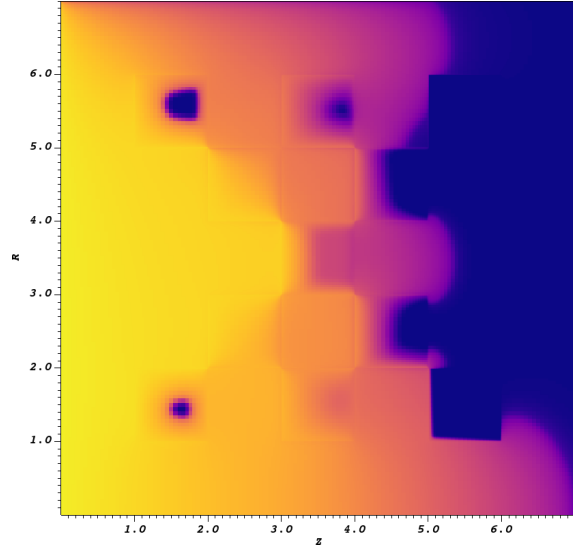


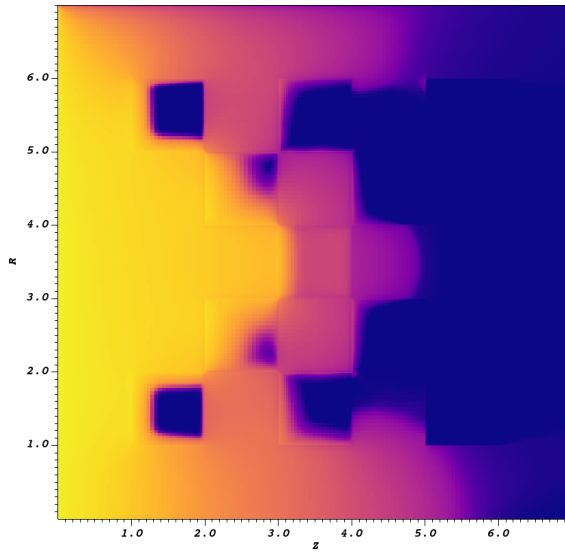
Figure 10: Linear scale radiation temperature at  $t = 2.6$  ns for each method



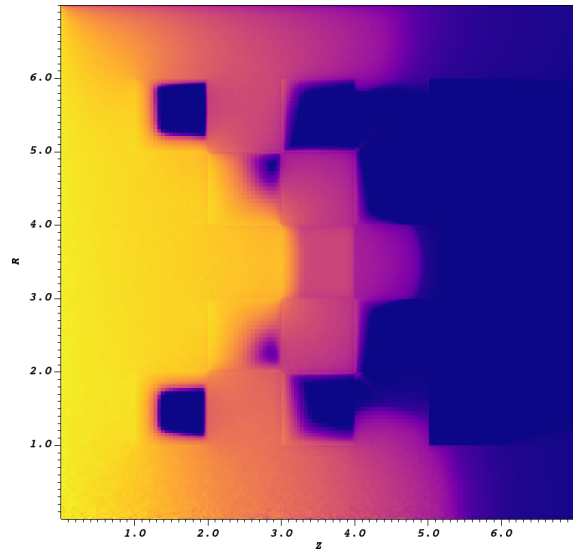
(a) FLD



(b) MGFLD



(c) S4x4



(d) IMC

Figure 11: Linear scale material temperature at  $t = 2.6$  ns for each method



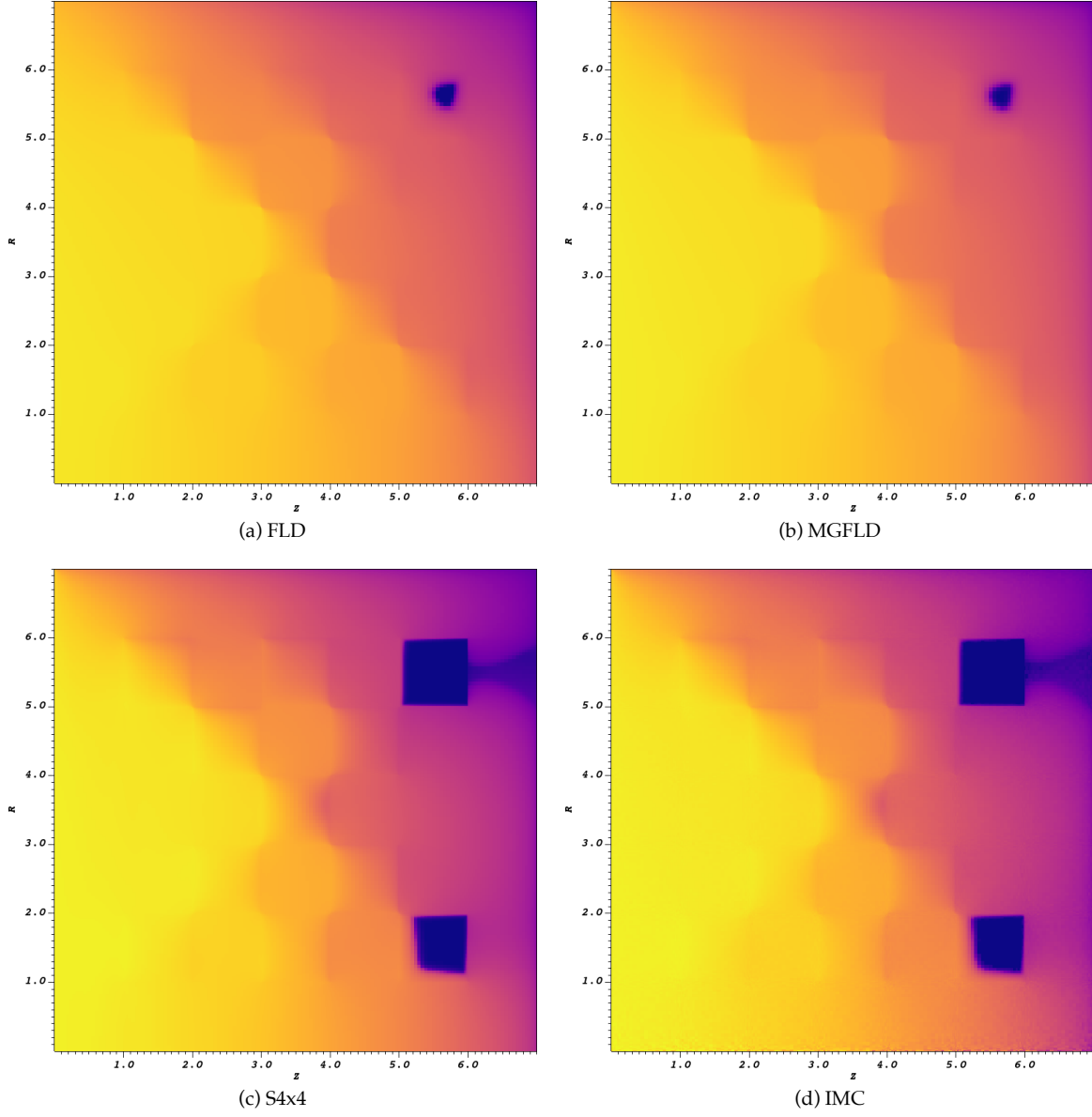
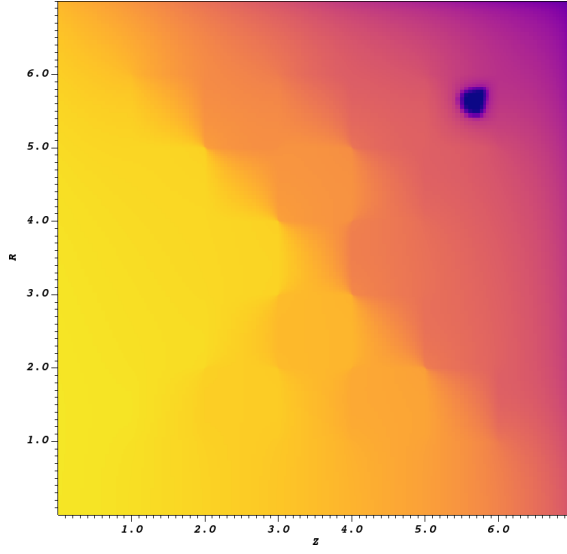
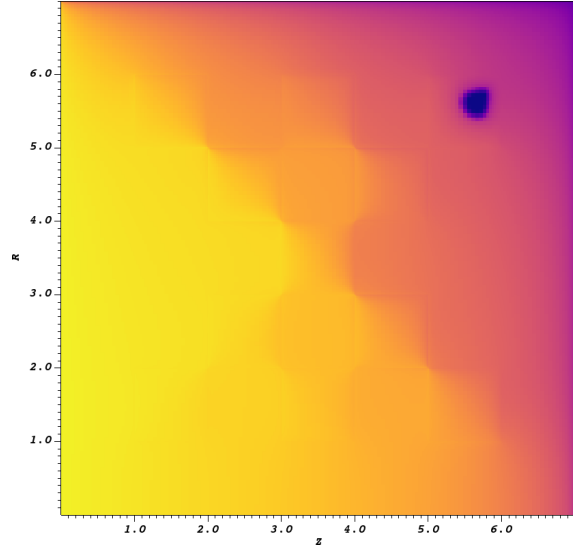


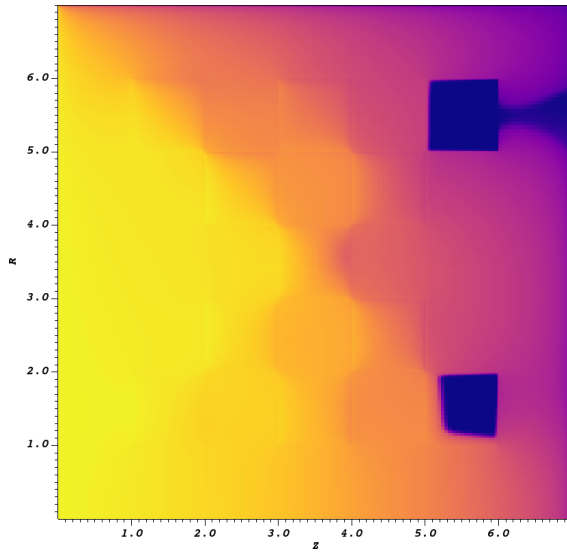
Figure 12: Linear scale radiation temperature at  $t = 15$  ns for each method



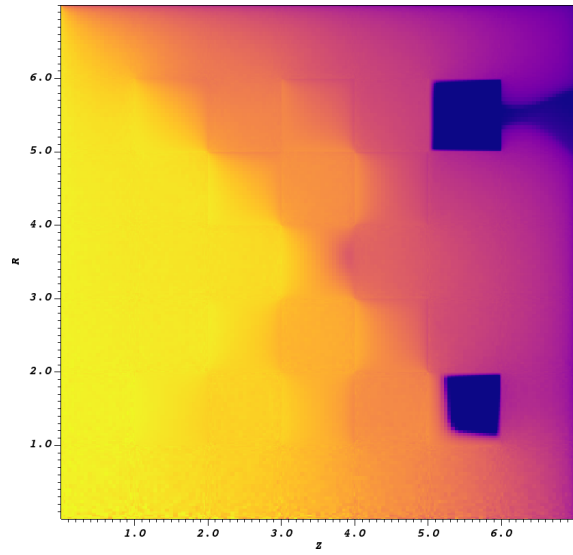
(a) FLD



(b) MGFLD

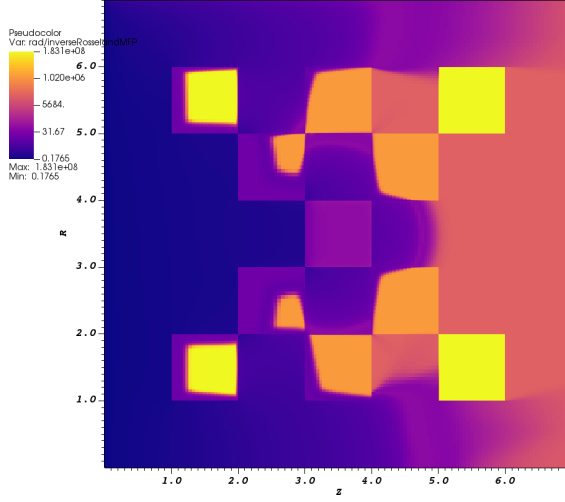


(c) S4x4

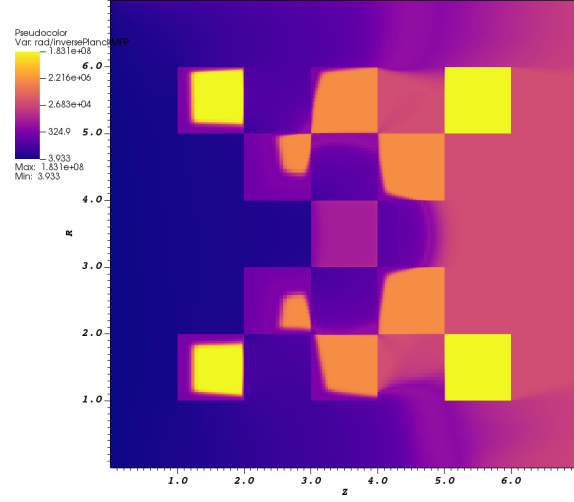


(d) IMC

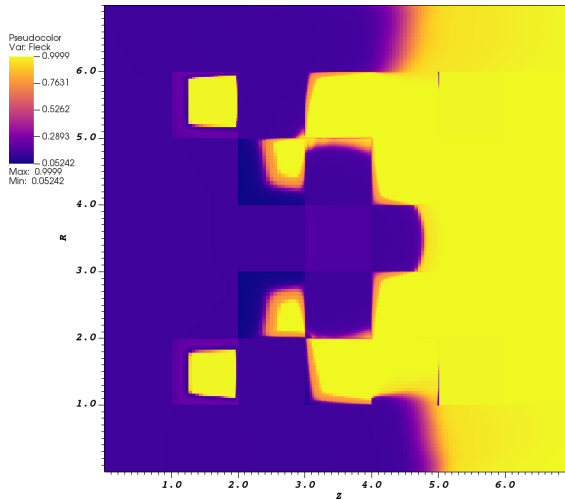
Figure 13: Linear scale material temperature at  $t = 15$  ns for each method



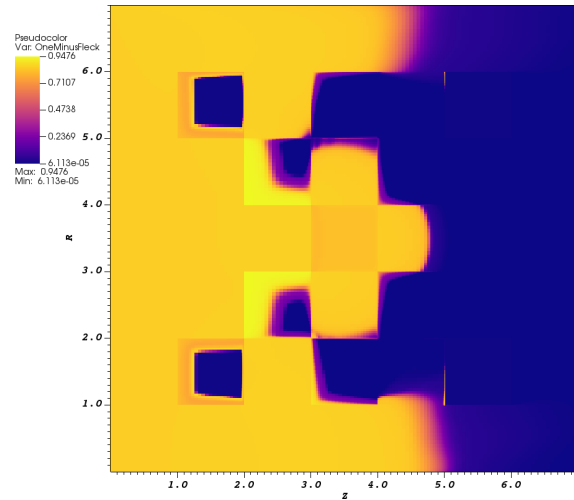
(a) Grey Rosseland opacity,  $\sigma_R$



(b) Grey Planck opacity,  $\sigma_P$

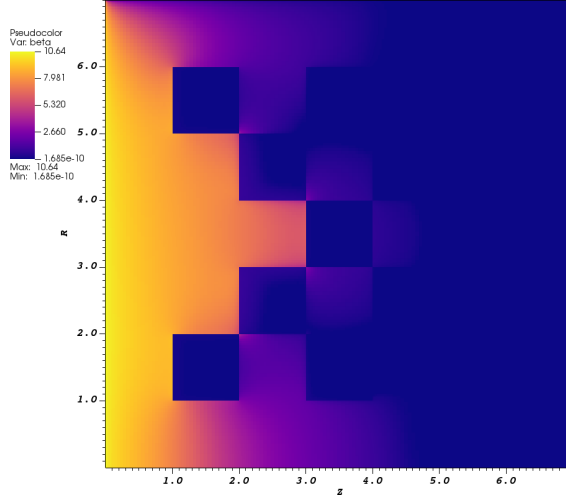


(c) Fleck factor  $f$ , Eq. 31

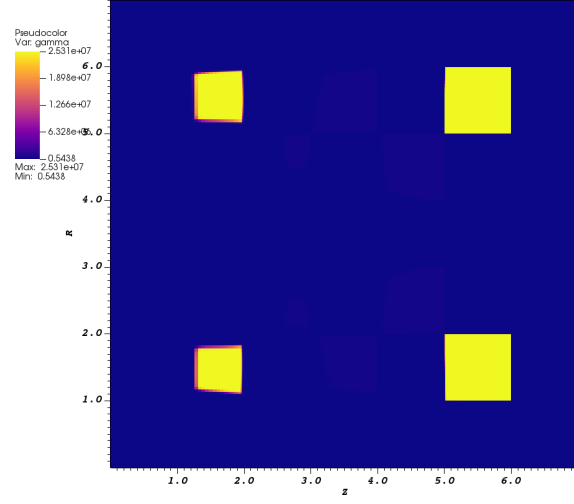


(d)  $1 - f$

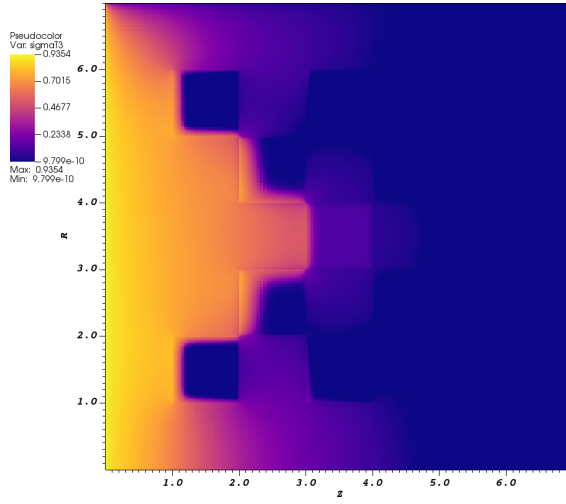
Figure 14: Other material properties at  $t = 1.5$  ns



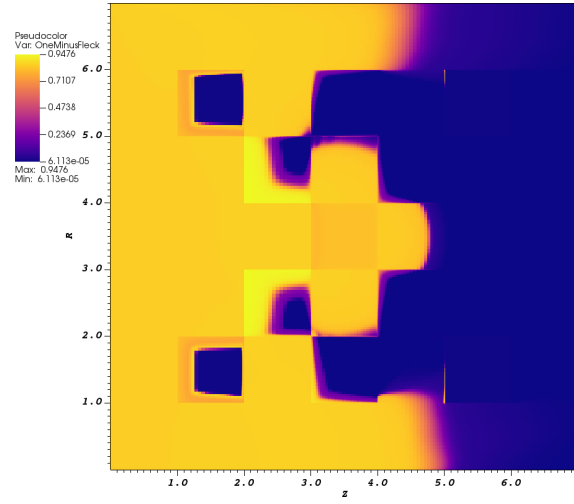
(a) heat capacity ratio  $\beta$ , Eq. 32



(b) path length ratio  $\gamma$ , Eq. 33



(c) relative re-emission  $\sigma_P T^3$



(d)  $1 - f$

Figure 15: Fleck factor components at  $t = 1.5$  ns

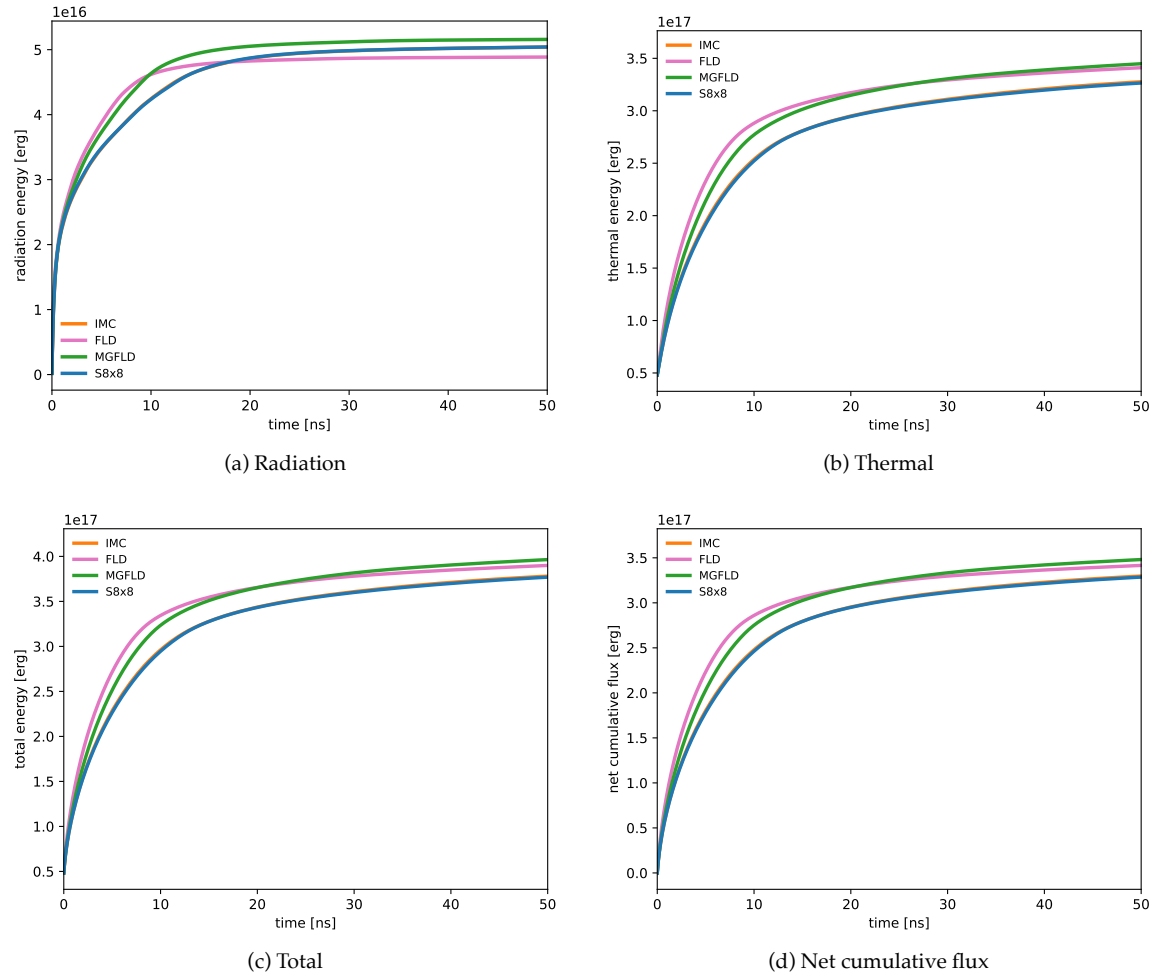


Figure 16: Radiation, thermal, and net flux of the energy summed over the entire problem.

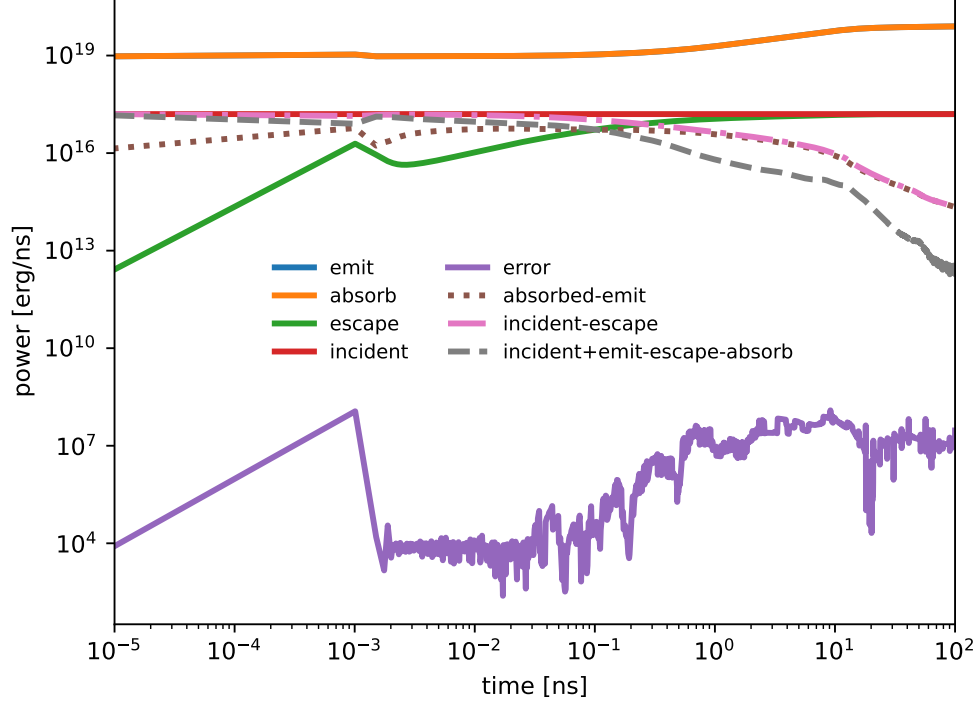


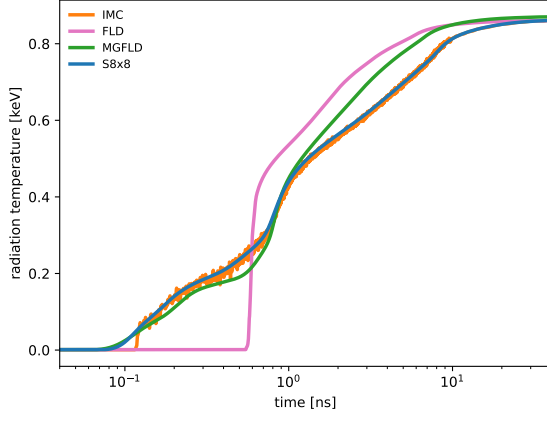
Figure 17: Mesh, energy, and angle integrated terms for Eq. 4 for the S8x8 simulation.

energy. Fig. 17 shows the instantaneous power balance of the mesh, energy, and angle integrated terms in Eq. 4. Our code can also keep a running tally of the error in energy balance that it has made; this has been extremely useful in finding bugs over the years. Note that many of the individual terms are very large and very nearly cancel each other to get the net change in energy to either the radiation (incident plus emit minus escape minus absorbed) or material fields (absorbed minus emitted).

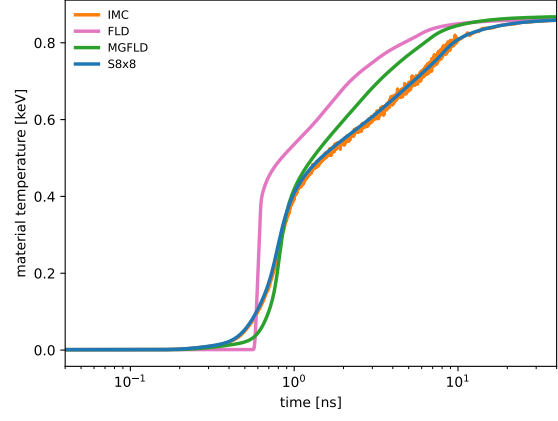
The color map plots of Figs. 8-13 are good for getting a qualitative feel for how the different methods are behaving. To more quantitatively compare the methods, we put tracer particles at various locations in the mesh which allow us to report quantities at those points as a function of time. Fig. 18 shows the radiation and material temperatures in the foam at the point  $r = 0.5$  cm,  $z = 3.5$  cm just near the axis. Fig. 8 showed a sharp edge for the IMC result, but diffuse wave front for the discrete ordinate and diffusion. Fig. 18 shows this as well, but here it is easier to see that after the initial front passes, the discrete ordinates and IMC results agree with each other, but the multigroup diffusion is different. Both diffusion methods initially under heat the material, only to over heat later in time.

The next point we will look at is in the middle of the lower block of cold iron located at  $r = 1.5$  cm,  $z = 1.5$  cm. Fig. 19 clearly shows the teleportation effect[19] in the IMC method. In thick materials, the IMC does not obey the diffusion limit and lets the radiation transport into the material faster than it should. This also happens in reverse too for thick hot materials that radiate. Fig. 20 shows the temperature history at the point in the middle of the hot iron block at  $r = 3.5$  cm,  $z = 3.5$  cm. The IMC has allowed the block to cool too much before the boundary source starts to heat it. Also visible in Fig. 19 bumps in the heating rate for the grey diffusion. This is a result of the grey opacity being non-monotonic due to the shell edges, as seen in Fig. 14. None of the multigroup simulations are susceptible to this behavior.

We next look at a point in the foam behind some of the thicker materials so it does not directly see any of the sources. Fig. 21 shows the temperature behavior at  $r = 5.5$  cm,  $z = 2.5$  cm. The diffusion methods allow too much radiation to unphysically bend around the objects. The IMC is also subject to some noise, but gets the arrival time correct. After the initial transient, the discrete ordinates and IMC results match very

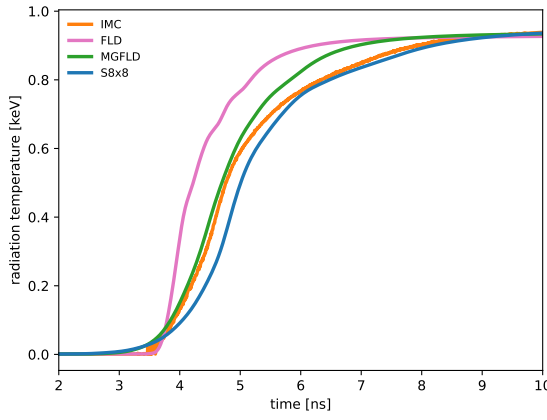


(a) radiation temperature

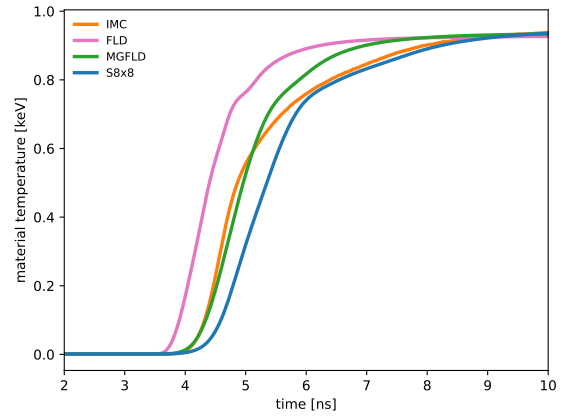


(b) material temperature

Figure 18: Temperatures at the point  $r = 0.5$  cm,  $z = 3.5$  cm versus time.



(a) radiation temperature



(b) material temperature

Figure 19: Temperatures at the point  $r = 1.5$  cm,  $z = 1.5$  cm versus time.

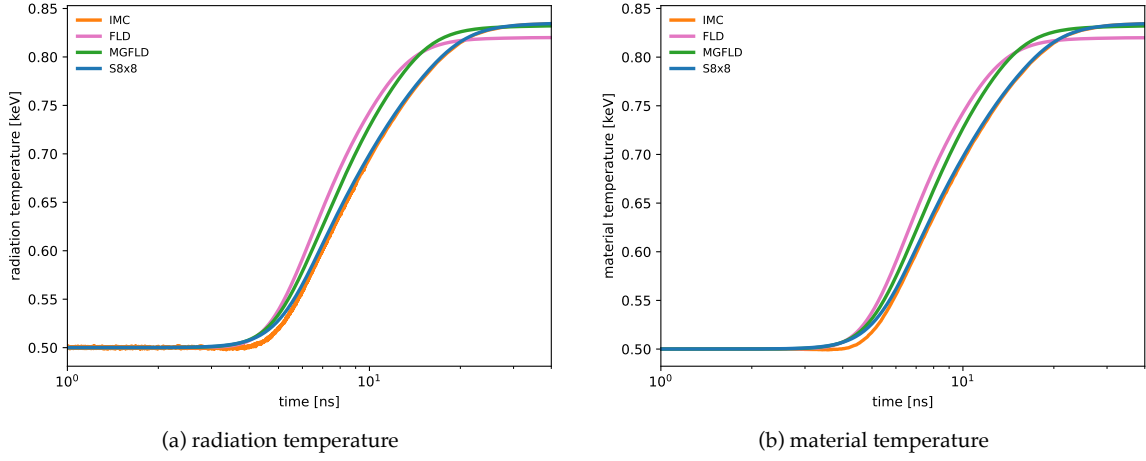


Figure 20: Temperatures at the point  $r = 3.5$  cm,  $z = 3.5$  cm versus time.

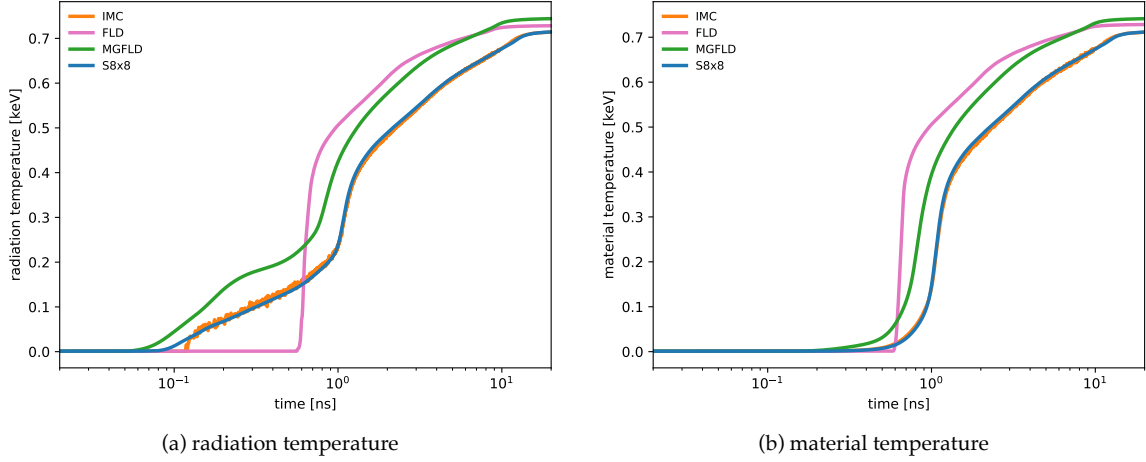


Figure 21: Temperatures at the point  $r = 5.5$  cm,  $z = 2.5$  cm versus time.

well. Fig. 22 shows the effect of the diffusion approximation's inability have shadows. The carbon block at  $r = 4.5$  cm,  $z = 4.5$  cm is essentially heated from all sides and warms up much too quickly relative to the transport-based methods.

## A Linearization

Eqs. 4-5 are nonlinear. Solution methods often involve some form of Newton or Newton-like iteration where the equations are linearized and solved iteratively. Details can be found in many sources, including [17, 13, 9, 15, 4]. After time discretizing using backward Euler, taking the Jacobian of the nonlinear system and eliminating the material temperature equation, Till [17] shows that we end up with the following



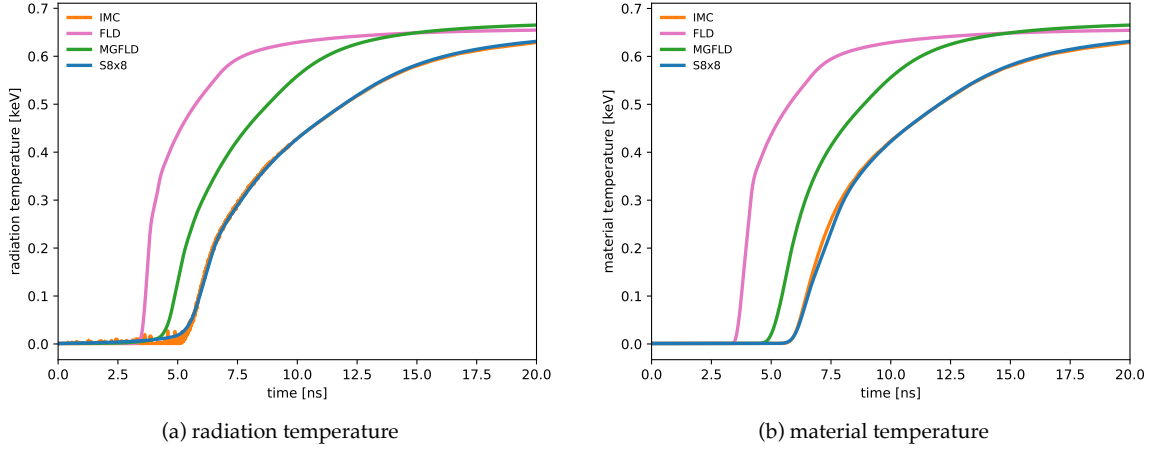


Figure 22: Temperatures at the point  $r = 4.5$  cm,  $z = 4.5$  cm versus time.

multigroup, steady-state transport equation

$$(\mathbf{\Omega} \cdot \nabla + \sigma_g + \tau) \psi_g = \frac{1}{4\pi} \alpha_g \sum_{g'} \sigma_{g'} \phi_{g'} + Q_g(\mathbf{\Omega}) \quad (28)$$

$$\alpha_g = \frac{4\pi \sigma_g \frac{\partial B_g}{\partial T}}{\frac{\rho c_v}{\Delta t} + 4\pi \sum_{g'} \sigma_{g'} \frac{\partial B_{g'}}{\partial T}} \quad (29)$$

$$Q_g(\mathbf{\Omega}) = \tau \psi_g^{n-1}(\mathbf{\Omega}) + \sigma_g B_g - \alpha_g \sum_{g'} \sigma_{g'} B_{g'} \quad (30)$$

and  $\tau = \frac{1}{c\Delta t}$ . Note that even though we did not start with scattering in the original system, the linearization procedure has created some effective scattering from the absorption and re-emission within the Newton step. These formulas can be used to create multigroup parameters for a steady state transport-only code. The group-to-group scattering is one of the key challenges for thermal radiation solvers and is important to include.

Often some algebra is done to rearrange terms. This leads to the Fleck factor, Eq. 4.1d in [9]. This is a measure of the fraction of photons that are absorbed and re-emitted within a step. It is written as

$$f = \frac{1}{1 + \beta c \Delta t \sigma_P} = \frac{1}{1 + \frac{4aT^3}{\rho c_v} c \Delta t \sigma_P}. \quad (31)$$

Note this is related to  $\alpha_g$  above by pulling the group-dependent numerator into another term. The fraction of photons absorbed and re-emitted is given by  $1 - f$ .

In Eq. 31, we can identify two other non-dimensional terms. The first can be thought of as the ratio of the radiation to material heat capacities, namely

$$\beta = \frac{4aT^3}{\rho c_v}. \quad (32)$$

The other is ratio of path length of a free streaming photon to the photons mean free path in the material, or

$$\gamma = c \Delta t \sigma_P. \quad (33)$$

The typical time steps for this calculation are shown in Fig. 23. Using a few different time step sizes and temperatures and Eqs. 28-30, it is possible to construct coefficients for a steady-state neutral particle transport code to test the linear solver method including strong group-to-group coupling that is representative of time-dependent TRT problems.

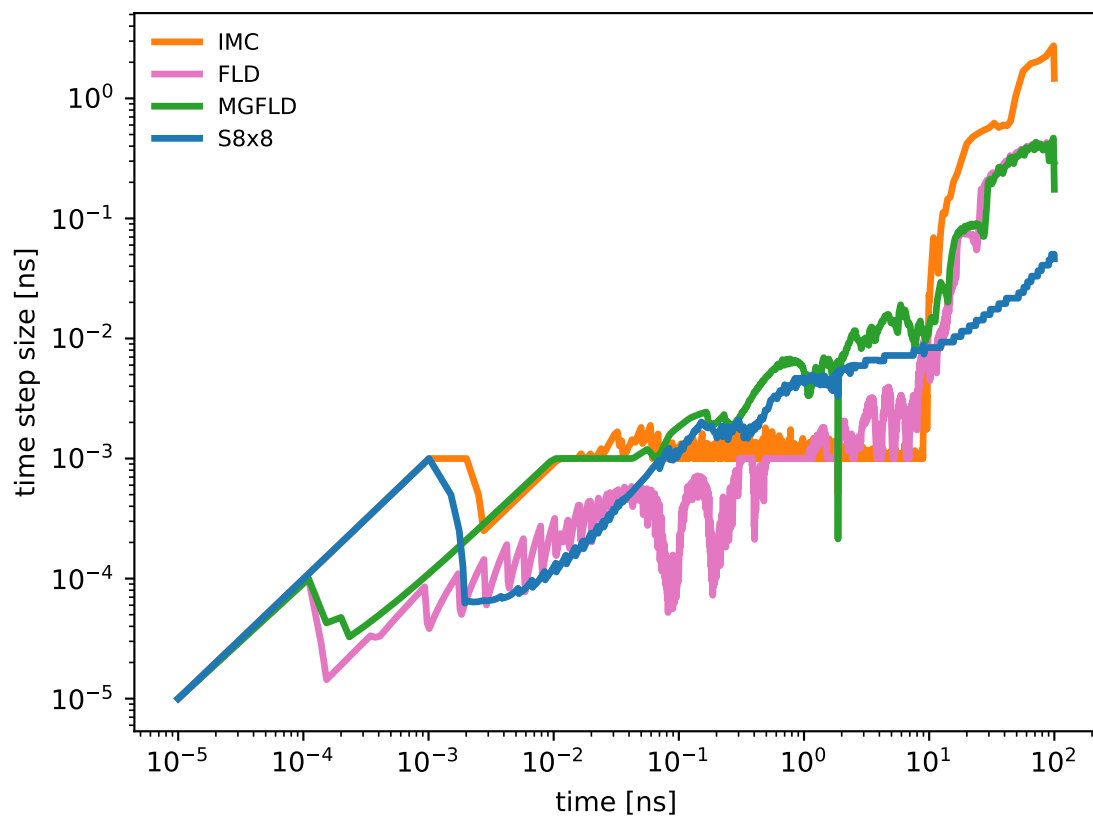


Figure 23: Typical time steps through the simulation.

## B Unit Conversion

The Planck function often appears as a function of temperature and photon frequency. In SI units, this looks like

$$B(\nu, \hat{T}) = \frac{2h\nu^3}{c^2} \frac{1}{\exp \left[ h\nu / \hat{k}_B \hat{T} \right] - 1}, \quad (34)$$

where  $B(\nu, \hat{T})$  is the Planck distribution (J/m<sup>2</sup> s Hz sr),  $\nu$  is the photon frequency (Hz),  $h$  is Planck's constant (J s),  $\hat{T}$  is the temperature (K),  $\hat{k}_B$  is Boltzmann's constant (J/K), and  $c$  is the speed of light (m/s).

We find it more convenient to express both the temperature and photon energy in the same units, namely keV. Changing most of the constants to other units can happen without any difficulty. But we'd like to introduce a new variable,  $\epsilon = h\nu / k_B$  into this equation. Before we proceed, we'll note that

$$\epsilon = \frac{h\nu}{k_B}, \quad (35)$$

$$\nu = \frac{k_B \epsilon}{h}, \quad (36)$$

$$d\epsilon = \frac{h}{k_B} d\nu, \text{ and} \quad (37)$$

$$d\nu = \frac{k_B}{h} d\epsilon. \quad (38)$$

Because the Planck function is differential in frequency, we need the energy in a small range to be the same. This implies

$$B(\epsilon, T) d\epsilon = B(\nu, T) d\nu \quad (39)$$

$$= \frac{2h\nu^3}{c^2} \frac{1}{\exp [h\nu / k_B T] - 1} d\nu \quad (40)$$

$$= B(\nu(\epsilon), T) d\nu \quad (41)$$

$$= \frac{2h}{c^2} \left( \frac{k_B \epsilon}{h} \right)^3 \frac{1}{\exp [\epsilon / T] - 1} d\nu \quad (42)$$

$$= \frac{2k_B^3}{c^2 h^2} \frac{\epsilon^3}{\exp [\epsilon / T] - 1} d\nu \quad (43)$$

$$= \frac{2k_B^4}{c^2 h^3} \frac{\epsilon^3}{\exp [\epsilon / T] - 1} d\epsilon \quad (44)$$

so finally we arrive at

$$B(\epsilon, T) d\epsilon = \frac{2k_B^4}{c^2 h^3} \frac{\epsilon^3}{\exp [\epsilon / T] - 1}. \quad (45)$$

We can now express these constants in any unit system as long as the main variables have the same base units (in terms of length, time, mass, etc.).

## C Alternative geometry

The geometry shown in Fig. 2 is only one possible arrangement of materials. Two more are presented here as alternatives. Some of the details and differences between the methods may be harder to see in these geometries, but the mesh is physically smaller, which might result in lower run times. While these geometries were explored early in the problem development, no results will be shown here. Fig. 24 shows two possible alternative geometries.

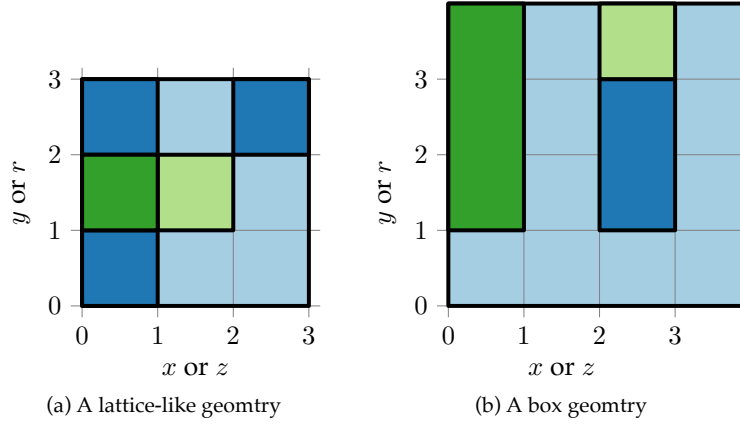


Figure 24: Two alternative geometries. Same boundary conditions and materials as in Fig. 2.

## D Acknowledgments

This work was performed under the auspices of the U.S. Department of Energy by Lawrence Livermore National Laboratory under Contract DE-AC52-07NA27344.

## References

- [1] “Los Alamos opacity on the World Wide Web.” Technical Report LA-UR-01-1257, Los Alamos, N.M., 2001. URL <https://aphysics2.lanl.gov/apps/>.
- [2] T. A. Brunner. “AnalyticMGOpac.” URL <https://github.com/LLNL/AnalyticMGOpac>.
- [3] T. A. Brunner. “Forms of Approximate Radiation Transport.” Technical Report SAND2002-1778, Sandia National Lab. (SNL-NM), Albuquerque, NM (United States), 6 2002. doi:10.2172/800993.
- [4] T. A. Brunner, T. S. Haut, and P. F. Nowak. “Nonlinear Elimination Applied to Radiation Diffusion.” *Nuclear Science and Engineering*, volume 194(11):pages 939–951, 2020. doi:10.1080/00295639.2020.1747262.
- [5] J. I. Castor. *Radiation hydrodynamics*. Cambridge University Press, Cambridge, UK, 2004.
- [6] B. Chang. “A deterministic photon free method to solve radiation transfer equations.” *Journal of Computational Physics*, volume 222(1):pages 71–85, 2007. ISSN 0021-9991. doi:10.1016/j.jcp.2006.06.048.
- [7] M. Cleveland and A. Wollaber. “Corrected implicit Monte Carlo.” *Journal of Computational Physics*, volume 359:pages 20–44, 2018. ISSN 0021-9991. doi:10.1016/j.jcp.2017.12.038.
- [8] J. Fleck and E. Canfield. “A random walk procedure for improving the computational efficiency of the implicit Monte Carlo method for nonlinear radiation transport.” *Journal of Computational Physics*, volume 54(3):pages 508–523, 1984. ISSN 0021-9991. doi:10.1016/0021-9991(84)90130-X.
- [9] J. Fleck and J. Cummings. “An implicit Monte Carlo scheme for calculating time and frequency dependent nonlinear radiation transport.” *Journal of Computational Physics*, volume 8(3):pages 313 – 342, 1971. ISSN 0021-9991. doi:10.1016/0021-9991(71)90015-5.

- [10] N. Gentile. “Implicit Monte Carlo Diffusion—An Acceleration Method for Monte Carlo Time-Dependent Radiative Transfer Simulations.” *Journal of Computational Physics*, volume 172(2):pages 543–571, 2001. ISSN 0021-9991. doi:10.1006/jcph.2001.6836.
- [11] F. Graziani. “The Prompt Spectrum of a Radiating Sphere: Benchmark Solutions for Diffusion and Transport.” In F. Graziani, editor, “Computational Methods in Transport: Verification and Validation,” pages 151–167. Springer Berlin Heidelberg, Berlin, Heidelberg, 2008. ISBN 978-3-540-77362-7.
- [12] F. Graziani and J. LeBlanc. “The crooked pipe test problem.” *Lawrence Livermore National Laboratory Report UCRL-MI-143393*, 2000.
- [13] E. Larsen. “A grey transport acceleration method for time-dependent radiative transfer problems.” *Journal of Computational Physics*, volume 78(2):pages 459–480, 1988. ISSN 0021-9991. doi:10.1016/0021-9991(88)90060-5.
- [14] R. G. McClarren, J. P. Holloway, and T. A. Brunner. “On solutions to the Pn equations for thermal radiative transfer.” *Journal of Computational Physics*, volume 227(5):pages 2864–2885, 2008. ISSN 0021-9991. doi:10.1016/j.jcp.2007.11.027.
- [15] J. E. Morel, T.-Y. B. Yang, and J. S. Warsa. “Linear multifrequency-grey acceleration recast for preconditioned Krylov iterations.” *Journal of Computational Physics*, volume 227(1):pages 244 – 263, 2007. ISSN 0021-9991. doi:10.1016/j.jcp.2007.07.033.
- [16] B. Su and G. L. Olson. “Non-grey benchmark results for two temperature non-equilibrium radiative transfer.” *Journal of Quantitative Spectroscopy and Radiative Transfer*, volume 62(3):pages 279–302, 1999. ISSN 0022-4073. doi:10.1016/S0022-4073(98)00105-8.
- [17] A. T. Till, J. S. Warsa, and J. E. Morel. “Application of linear multifrequency-grey acceleration to preconditioned Krylov iterations for thermal radiation transport.” *Journal of Computational Physics*, volume 372:pages 931 – 955, 2018. ISSN 0021-9991. doi:10.1016/j.jcp.2018.06.017.
- [18] Wikipedia contributors. “Gaussian function — Wikipedia, The Free Encyclopedia.” [https://en.wikipedia.org/w/index.php?title=Gaussian\\_function&oldid=1171566379](https://en.wikipedia.org/w/index.php?title=Gaussian_function&oldid=1171566379), 2023. [Online; accessed 7-November-2023].
- [19] A. B. Wollaber. “Four Decades of Implicit Monte Carlo.” *Journal of Computational and Theoretical Transport*, volume 45(1-2):pages 1–70, 2016. doi:10.1080/23324309.2016.1138132.
- [20] Y. B. Zel’Dovich and Y. P. Raizer. *Physics of shock waves and high-temperature hydrodynamic phenomena*. Courier Corporation, 2002.